



Sodium Charge Storage in Thin Films of MnO₂ Derived by Electrochemical Oxidation of MnO Atomic Layer Deposition Films

Matthias J. Young,^a Markus Neuber,^b Andrew C. Cavanagh,^{b,*} Huaxing Sun,^b Charles B. Musgrave,^{a,b} and Steven M. George^{b,c,*}

^aDepartment of Chemical and Biological Engineering, University of Colorado, Boulder, Colorado 80309, USA

^bDepartment of Chemistry and Biochemistry, University of Colorado, Boulder, Colorado 80309, USA

^cDepartment of Mechanical Engineering, University of Colorado, Boulder, Colorado 80309, USA

Sodium charge storage in ultrathin MnO₂ films was studied using cyclic voltammetry (CV) and electrochemical quartz crystal microbalance (EQCM) measurements. The MnO₂ films were fabricated by electrochemical oxidation of MnO films grown by atomic layer deposition (ALD). CV analysis confirmed that oxidation of MnO to MnO₂ involved two moles of electrons per mole of Mn in the MnO ALD film. Scanning electron microscopy (SEM) images revealed that electrochemical oxidation of MnO led to the formation of MnO₂ nanosheets. EQCM measurements suggested that Na⁺ cations participate in charge storage in MnO₂. X-ray photoelectron spectroscopy (XPS) experiments measured sodium in MnO₂ after both positive/anodic and negative/cathodic voltage sweeps. The stoichiometry was Na_{0.25}MnO₂ after negative/cathodic voltage sweeps. Approximately one-half of the sodium was removed after positive/anodic voltage sweeps. The areal capacitance increased progressively with initial MnO ALD film thickness. This increase in areal capacitance is consistent with bulk charge storage in MnO₂ or higher surface area of MnO₂ nanosheets resulting from larger MnO ALD film thicknesses. Experiments at varying scan rates indicated that charge storage in MnO₂ originates from a combination of capacitive and diffusive processes. Bulk charge storage makes a significant contribution to total charge storage in the thicker MnO₂ films.

© The Author(s) 2015. Published by ECS. This is an open access article distributed under the terms of the Creative Commons Attribution Non-Commercial No Derivatives 4.0 License (CC BY-NC-ND, <http://creativecommons.org/licenses/by-nc-nd/4.0/>), which permits non-commercial reuse, distribution, and reproduction in any medium, provided the original work is not changed in any way and is properly cited. For permission for commercial reuse, please email: oa@electrochem.org. [DOI: 10.1149/2.0671514jes] All rights reserved.

Manuscript submitted July 16, 2015; revised manuscript received October 1, 2015. Published October 21, 2015.

The energy and power density performance of electrochemical supercapacitors lies between lithium ion batteries and conventional capacitors.^{1,2} Compared with lithium ion batteries, electrochemical supercapacitors charge faster, but have a lower energy density. Compared with conventional capacitors, electrochemical supercapacitors can store more energy, but have a slower charge rate. Electrochemical supercapacitors also have extraordinary cycling stability and can maintain >90% of their capacity for 100,000s of cycles.³ The impressive charging rate capability, energy storage and stability of electrochemical supercapacitors makes them appealing for grid-level energy storage, buffering power generation from wind turbines and photovoltaics, and as a power buffer for regenerative braking technology.

Electrochemical supercapacitor materials exhibit a nearly constant capacitance over a wide potential region. This corresponds to a linear plot of transferred charge (Q) versus potential (V) ($C = \frac{dQ}{dV}$). This behavior is expected for chemically inert, high surface area conductive electrodes where charge is stored in the electric double layer at the electrode-electrolyte interface. Some redox-active materials also exhibit this behavior which leads to their description as “pseudocapacitors.” A wide variety of pseudocapacitive metal oxides have been reported, including MnO₂,^{4,5} Mn₂O₃,³ MoO₃,⁶ NiOH,⁷ RuO₂,⁸ SnO₂,⁹ TiO₂,¹⁰⁻¹² V₂O₅,¹³⁻¹⁵ ZnO,^{16,17} and others.¹⁸ However, only a few of these materials display a linear relationship between Q and V. The best known examples of true pseudocapacitive materials are ruthenium oxide and manganese oxide.^{1,2,19} Of these, manganese oxide is particularly appealing due to the low cost and earth-abundance of manganese.

A wide range of physical phenomena are involved in pseudocapacitive charge storage in MnO₂. Of the many stoichiometries and crystal structures of manganese oxide, only the α-MnO₂ and δ-MnO₂ crystal structures have been shown to exhibit pseudocapacitance with capacitances >200 F/g.^{20,21} Both crystal structures exhibit charge storage from 0–1 V versus Ag/AgCl in aqueous electrolyte at neutral pH.²⁰ One of the most notable observations for MnO₂ is an exceptionally high specific capacitance of >1,000 F/g when MnO₂ is blended with carbon powder at low mass loadings⁴ or deposited as a thin film.²²

Typical specific capacitances reported for larger mass loadings or “bulk” MnO₂ in aqueous electrolyte are ~200 F/g.²¹

The identity of the species responsible for charge storage in pseudocapacitive MnO₂ is uncertain. While protons are believed to be responsible for near-surface capacity,⁴ larger cations (Li⁺, Na⁺, and K⁺) are thought to contribute to the bulk capacity.²³⁻²⁷ In general, the capacity of electrochemical supercapacitor materials is believed to arise primarily from surface or near-surface proton-mediated processes. In contrast, bulk charge storage is thought to add little to the total capacity.^{4,28} Based on these expectations, the capacitance should scale with the surface area of the electrode material. However, previous studies have determined that the specific mass capacitance does not correlate with the specific surface area.^{20,21} In addition, recent theoretical work predicted that charge storage in α-MnO₂ results from “charge-switching” interstitial and substitutional cations in α-MnO₂.²⁷

In this work, we study charge storage in MnO₂ films. The MnO₂ films were prepared by electrochemically oxidizing MnO films with precise initial thicknesses that were grown using atomic layer deposition (ALD). The identity of the species that stores charge in MnO₂ was explored using electrochemical quartz crystal microbalance (EQCM) and X-ray photoelectron spectroscopy (XPS) measurements. The electrochemical charge storage in MnO₂ films was investigated for different MnO₂ film thicknesses and sweep rates using cyclic voltammetry (CV) studies. These CV studies enable the charge storage in MnO₂ to be understood in terms of capacitive and diffusive contributions. These results illustrate that Na⁺ ions in the bulk of MnO₂ make a sizable contribution to the total charge storage of MnO₂.

Experimental

Sample preparation and ALD growth.— The direct growth of MnO₂ by ALD is difficult.^{29,30} In contrast, MnO ALD is a very robust ALD system.³¹ MnO₂ films were prepared using MnO ALD and subsequently electrochemically oxidized to MnO₂. The MnO ALD was performed on optically flat 430 stainless steel (SS) discs with a surface roughness of ~20 Å. Electron discharge machining was used to cut 5 in. diameter SS wafers (Valley Design) with a thickness of 500 μm into 5/8 in. diameter SS samples. These electrically

*Electrochemical Society Active Member.

[†]E-mail: Steven.George@colorado.edu

conductive SS samples allowed for electrochemical characterization of the manganese oxide films.

Silicon samples with dimensions of $\sim 1'' \times 1''$ were cut from 6'' silicon wafers (Silicon Valley Microelectronics). These Si witness wafers were placed in the ALD reactor along with the SS discs during the film deposition. The SS and Si samples were both rinsed with acetone (Fisher, Certified ACS) and methanol (EMD Millipore HPLC grade). The samples were then blown dry using ultra high purity nitrogen (Airgas), and loaded into the ALD reactor. The samples were also cleaned in situ with a water plasma using ~ 300 mTorr of water pressure for 30–60 seconds prior to ALD growth.

The ALD was performed simultaneously on the SS and Si samples at 150°C and ~ 1 Torr under a 120 sccm continuous argon (Ar) gas purge (Airgas, Prepurified). The ALD was conducted in a custom viscous-flow reactor.³² MnO was deposited using sequential exposures of (A) bis(ethylcyclopentadienyl) manganese ($\text{Mn}(\text{CpEt})_2$) ($>98\%$, Strem Chemicals) and (B) water (H_2O) (B&J Brand HPLC Grade) as described previously.³¹

$\text{Mn}(\text{CpEt})_2$ was dosed with the Ar gas flow directed over the head-space of the $\text{Mn}(\text{CpEt})_2$ bubbler during dosing. Peak dose pressures of H_2O were tuned to ~ 200 mTorr above base pressure. The timing sequence used for one A: Purge: B: Purge ALD cycle was 0.5 s: 20 s: 0.5 s: 20 s.

Electrochemical oxidation and evaluation.— The MnO ALD films were electrochemically oxidized and evaluated using a 2-channel SP-300 potentiostat with low current probes from BioLogic. Following growth of the MnO ALD films, the SS samples were loaded into a custom 3-electrode cell for electrochemical evaluation. Only a portion of the MnO ALD surface was exposed to the electrolyte. This exposed area was defined by an o-ring seal on the sample surface. Fresh 0.10 M $\text{Na}_2\text{SO}_{4(\text{aq})}$ (Alfa Aesar, 99.99% metals basis) electrolyte was used for analysis of each sample using a platinum counter electrode and saturated Ag/AgCl reference electrode (BASi).

After filling the electrochemical cell with electrolyte, the cell was purged with Ar gas (Airgas, Prepurified) for >10 minutes, and kept under a continuous Ar gas purge during the measurements. A two-step process was repeated for each sample to measure the charge storage properties during oxidation. First, three successive CV loops were performed between 0.0 V and 0.9 V versus Ag/AgCl at a sweep rate of $\nu = 20$ mV/s. Subsequently, the sample was oxidized at a constant current of 10 μA at a potential of up to 1.2 V for two minutes.

These two steps were repeated until oxidation of the MnO ALD film was complete. Complete oxidation corresponded with an integrated oxidation current of at least $2 e^-/\text{Mn}$ resulting from the reaction $\text{Mn}^{2+} \rightarrow \text{Mn}^{4+} + 2e^-$. In addition, the capacitance from CV measurements did not increase after complete oxidation. After oxidation, further CV experiments were performed at scan rates of $5 \leq \nu \leq 400$ mV/s to evaluate the kinetics of the processes contributing to charge storage.

Electrochemical quartz crystal microbalance.— MnO was deposited by ALD on a gold-plated EQCM crystal (Stanford Research Systems QCM25). These EQCM crystals were then loaded into a standard crystal holder (Stanford Research Systems) and placed in a custom electrochemical cell. Similar to the CV measurements described above, a 0.1 M Na_2SO_4 aqueous electrolyte, platinum counter electrode, and saturated Ag/AgCl reference electrodes were used for electrochemical analysis.

Electrochemical oxidation and analysis were performed in the same manner as described for MnO films deposited on SS samples. The mass change in the manganese oxide film during electrochemical analysis was measured using a QCM200 Quartz Crystal Microbalance (Stanford Research Systems). The QCM200 QCM was connected directly to the BioLogic potentiostat for data acquisition and recording.

X-ray reflectivity and X-ray diffraction.— X-ray reflectivity (XRR) was used to determine the thicknesses and densities of the MnO ALD coatings on the Si and SS samples. A Bede D-1 Diffractometer (Jor-

dan Valley Semiconductors) was used to perform XRR measurements. X-ray radiation with a wavelength of 1.54 Å was used for these measurements. This X-ray wavelength corresponds to the Cu-K α transition from the Cu anode. Film thicknesses and densities were modeled using the Bede REFS software package (Jordan Valley Semiconductors).

Glancing Incidence X-ray Diffraction (GIXRD) was utilized to evaluate film crystallinity using the Bede D-1 Diffractometer. X-ray radiation with a wavelength of 1.54 Å was used for the measurements. The glancing incidence angle, ω , was set to 0.5° which is just above the critical angle measured for manganese oxide films by XRR. The step size was ≤ 0.05 degrees for every XRD measurement, and the count time was ≥ 20 seconds.

The XRD spectra were compared with simulated powder XRD spectra of experimental Inorganic Crystal Structure Database (ICSD)³³ crystal structures. These crystal structures are available from the Materials Project database.³⁴ XRD analysis used the RIETAN-FP·VENUS³⁵ package as implemented in VESTA.³⁶

X-ray photoelectron spectroscopy.— Following the electrochemical oxidation of MnO to MnO_2 defined by $\sim 2 e^-/\text{Mn}$ in 0.1 M Na_2SO_4 , the samples were dried at ambient conditions for >24 hours. Subsequently, $\sim 0.3'' \times 0.3''$ samples were cut from the MnO_2 -covered stainless steel disc and loaded into the XPS analysis chamber. A PHI 5600 X-ray photoelectron spectrometer was employed with monochromatic Al K α X-rays at an energy of 1486.6 eV.

Depth profiles were obtained by acquiring XPS spectra after intervals of Ar ion milling where the ion beam was rastered over the sample for 1 minute intervals. XPS spectra were acquired between sputtering intervals using a pass energy of 29.35 eV and a step size of 0.250 eV. An electron beam neutralizer was employed at 17.8 mA. Data was obtained with the Auger Scan control program (RBD Instruments) and analyzed using CASA XPS software (Casa Software).

Spectroscopic ellipsometry and scanning electron microscopy.— The thickness, optical bandgap, and refractive index of MnO-ALD films on the Si and SS samples were evaluated using spectroscopic ellipsometry (SE). SE measurements were performed using a spectroscopic ellipsometer (M-2000, J.A. Woollam Co., Inc.) over a spectral range of 240 nm to 1685 nm with a 75° incident angle. Film properties were evaluated using CompleteEASE v.4.55 (J.A. Woollam Co., Inc.). This evaluation used a Kramers-Kronig consistent B-spline model for the SS samples, silicon and silicon oxide materials files for the Si with native oxide, and a Cody-Lorentz model for the MnO ALD films. ALD film thicknesses by SE were benchmarked against XRR measurements on the Si and SS samples.

Manganese oxide films on SS samples were imaged before and after oxidation using scanning electron microscopy (SEM). The SEM instrument was a JEOL JSM-7401F field emission SEM set to a 5.0 kV accelerating voltage and a working distance of 2.4 mm.

Results and Discussion

MnO growth on silicon and stainless steel samples.— The MnO film thicknesses on Si samples measured by XRR and SE versus number of MnO ALD cycles are shown in Figure 1. The MnO ALD growth rate was 1.15 Å/cycle determined from both the XRR and SE measurements. This growth rate was also obtained by SE measurements after 1000 and 2000 MnO ALD cycles. This MnO ALD growth rate agrees with the growth rates measured in previous studies of MnO growth by ALD using the same $\text{Mn}(\text{CpEt})_2/\text{H}_2\text{O}$ ALD chemistry at 150°C .³¹ The growth rate on SS samples from XRR analysis was 0.95 Å/cycle, in reasonable agreement with the growth rate on Si samples.

The MnO films on SS samples were also studied using SE. The SE film thicknesses agree closely with the film thicknesses from the XRR measurements. Fitting based on a Cody-Lorentz model for all sample thicknesses resulted in a bandgap of 3.5 eV. This bandgap agrees

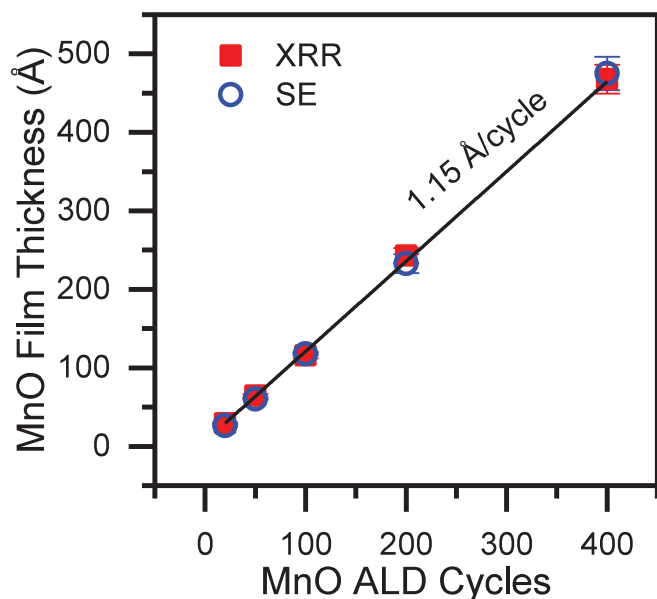


Figure 1. MnO ALD film thickness as measured by XRR and SE versus number of Mn(CpEt)₂/H₂O MnO ALD cycles on silicon samples. Both XRR and SE results yield a MnO ALD growth rate of 1.15 Å/cycle.

well with values of 3.5–3.8 eV reported for crystalline MnO.^{37,38} The refractive index from SE analysis shown in Figure 2 also indicates crystalline MnO. The refractive index from SE was 2.16 at 589 nm. This refractive index agrees with values of 2.11–2.22 at 589 nm reported previously for MnO and is significantly different from the refractive indexes of other manganese oxides.^{39,40}

Electrochemical oxidation.— The charge-storage capacity increases during electrochemical oxidation of the MnO ALD films. Figure 3 shows the cyclic voltammetry scans at a 20 mV/s sweep rate during various stages of oxidation. The area under the CV curves corresponds to the total capacity. As the MnO film undergoes oxidation, the film changes from a slightly tinted uniform transparent film to

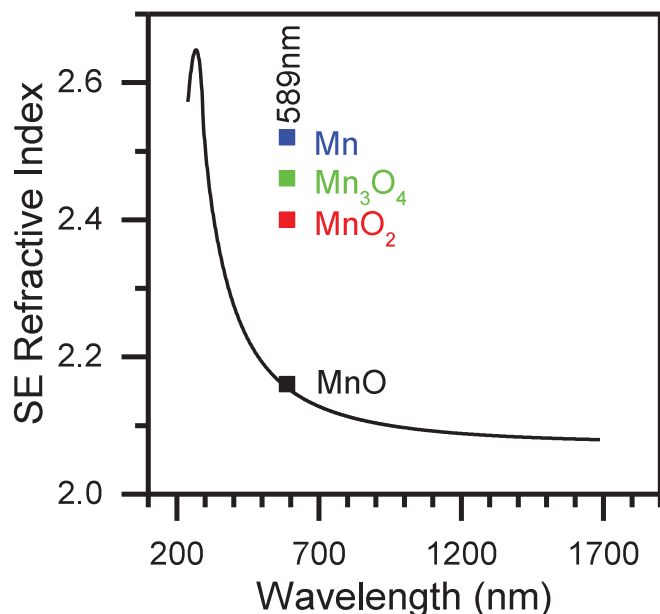


Figure 2. Refractive index versus wavelength for a model fit of all measured MnO ALD films grown using 20–2000 MnO ALD cycles.

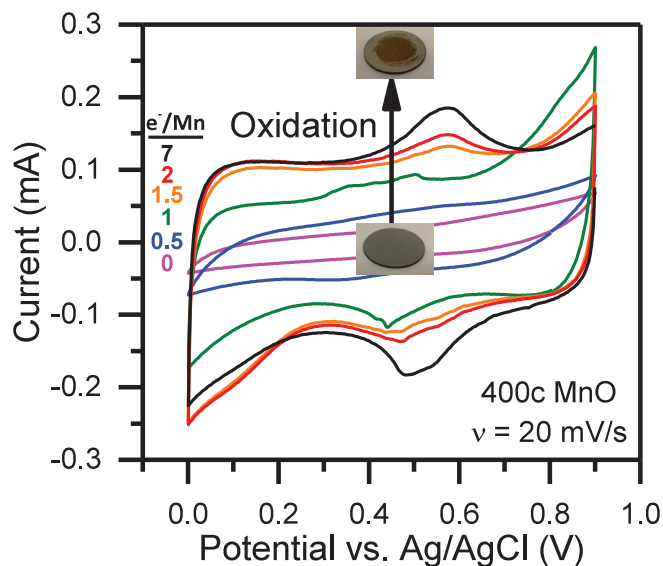


Figure 3. CV scans at 20 mV/s during the electrochemical oxidation of a MnO ALD film grown using 400 MnO ALD cycles. The inset photographs show that the MnO ALD film turns red-brown upon oxidation to MnO₂.

an opaque red-brown colored film. This color change is depicted in the inset photographs in Figure 3. The portion of the film that turned red-brown corresponds to the film exposed to the electrolyte during electrochemical measurements. The exterior edge of the film was not exposed to the electrolyte during oxidation and remains MnO.

The amount of Mn present in the initial MnO film was calculated for each sample using the film thickness and density determined by XRR before oxidation. After 2 e⁻/Mn of oxidation, the Mn²⁺ present in the initial MnO film should have all oxidized to Mn⁴⁺. Upon completion of oxidation, subsequent CV cycles become more rectangular in shape as expected for charge storage in electrochemical supercapacitors. The CV peak that appears at ~0.5 V versus Ag/AgCl upon oxidation beyond 2e⁻/Mn agrees with previous measurements of manganese oxide preintercalated with sodium.⁴¹ This CV peak corresponds to the charge storage of cations in Mn vacancies.²⁷ The appearance of this peak suggests that further oxidation leads to Mn vacancies that contribute additional capacity.^{27,42}

CV scans were performed while oxidizing MnO films of various thicknesses to determine how the film capacity depends on initial MnO film thickness. Figure 4 shows the increase in specific mass capacitance at 20 mV/s during oxidation for various initial thicknesses of MnO. The specific mass capacitances were calculated using the amount of Mn present in each MnO film as determined using the XRR thicknesses and densities. All of the initial MnO was assumed to be converted to MnO₂ after oxidation.

An analysis of the electrolytes after oxidation using inductively-coupled plasma mass spectrometry (ICP-MS) indicated that some of the Mn dissolves into the electrolyte during oxidation. The dissolution could correspond to as much as ~10 nm of the MnO ALD film. Dissolution of significant portions of the films was observed in some experiments for films with thicknesses ≤ 10 nm. This dissolution resulted in a dramatic drop in capacitance. Additionally, for initial Mn ALD films grown using 1,000 and 2,000 MnO ALD cycles with thicknesses of ~100 and ~200 nm, respectively, some particulate was observed in the electrolyte after oxidation. Because the determination of the specific mass capacitance neglected these losses, the calculated capacitances represent lower limits to the capacitance.

The XPS measurements also indicate that some of the near-surface MnO oxidizes to MnO₂ upon exposure to air prior to the electrochemical oxidation. This surface oxidation would affect the results shown in Figure 4 and leads to a plateau in capacitance with less than 2 e⁻/Mn of oxidation. Despite these possible sources of error,

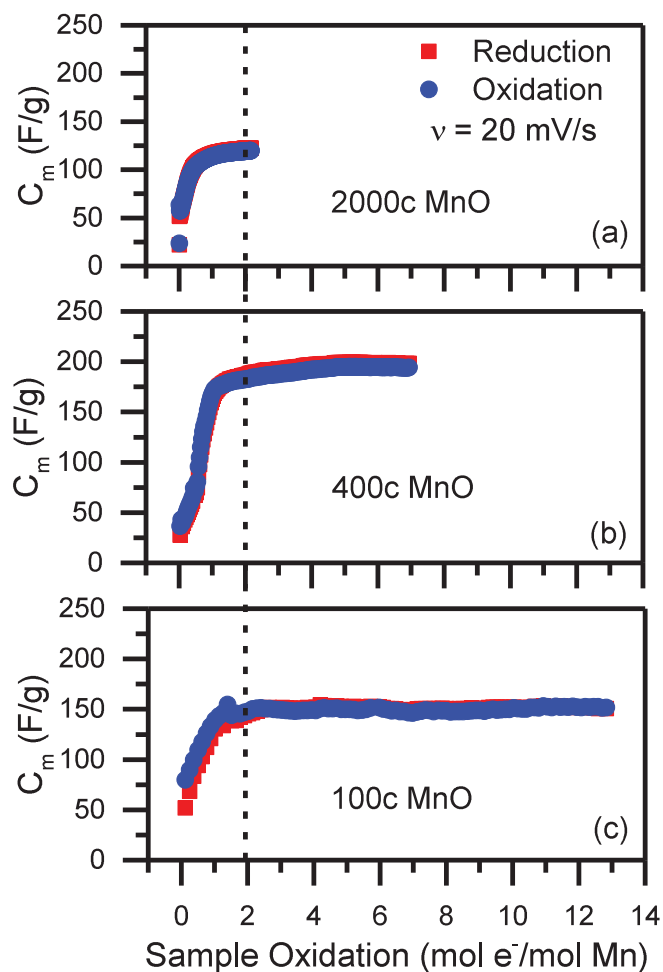


Figure 4. Specific mass capacitance versus oxidation in units of ($\text{mol e}^-/\text{mol Mn}$) for MnO_2 films formed from MnO ALD films grown using 100, 400 and 2000 cycles of ALD MnO. The capacitance was measured from CV scans at 20 mV/s. The capacitance plateaus at roughly $2 \text{ e}^-/\text{Mn}$.

Figure 4 shows that the capacitance for each sample reaches a plateau after $\sim 2 \text{ e}^-/\text{Mn}$ of oxidation.

Capacitance values on the order of $\sim 150\text{--}180 \text{ F/g}$ at 20 mV/s in Figure 4 agree with values previously reported for the $\alpha\text{-MnO}_2$ and $\delta\text{-MnO}_2$ phases.^{20,21} Previous results have demonstrated the formation of $\delta\text{-MnO}_2$ from electrochemical oxidation of Mn_3O_4 under similar electrochemical conditions.⁴³ The XRD measurements suggest that the electrochemically oxidized MnO ALD films are amorphous. In contrast, the XRD spectra of the as-grown MnO ALD films closely match crystalline MnO in agreement with prior results on MnO ALD.³¹

After the oxidation to MnO_2 is complete, the capacitance remains relatively constant upon further oxidation for each ALD thickness. The data in Figure 4 were recorded for 600 charge-discharge cycles and demonstrate good cycling stability even under intermediate oxidizing overpotentials. Some of the current after complete oxidation to MnO_2 may result in the production of Mn vacancies that produce a peak at 0.5 V vs Ag/AgCl. The remaining additional oxidation current is attributed to water-splitting to produce O_2 and H^+ as supported by the observation of bubbles on the electrode surface. There also could be dissolution of the MnO_2 to MnO_4^- as implied by Mn observed in the electrolyte by ICP-MS following electrochemical oxidation.

Species involved in charge storage from EQCM.— An EQCM trace for a MnO_2 film formed from an initial MnO ALD film grown using 200 ALD cycles is shown in Figure 5. The mass change is Δm and the

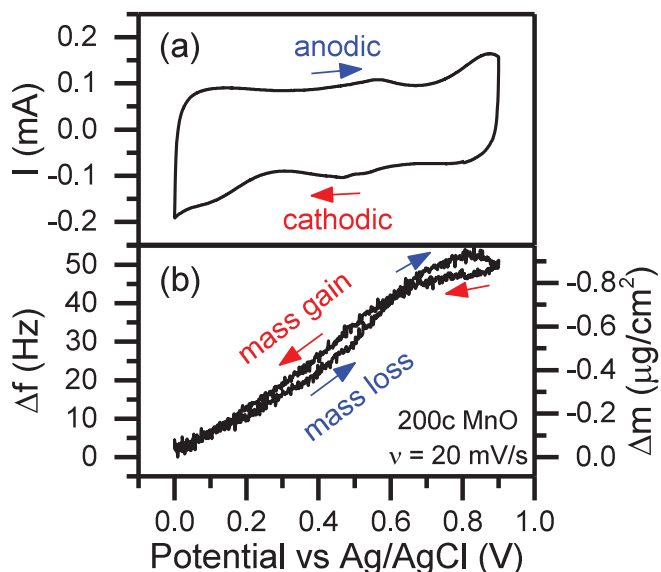


Figure 5. EQCM measurement of a MnO_2 film after oxidation of a MnO film deposited using 200 MnO ALD cycles. (a) CV scan at 20 mV/s and (b) QCM measurement of Δf and Δm corresponding to the CV scan at 20 mV/s.

resonant frequency change is Δf . As the potential is swept at 20 mV/s in the positive (anodic/oxidizing) direction, the current in Figure 5a is positive (loss of electrons from the electrode). Corresponding with this anodic current, the resonant frequency of the EQCM in Figure 5b increases (loss of mass from the electrode). As the potential is swept at 20 mV/s in the negative (cathodic/reducing) direction, the current is negative (gain of electrons into the electrode). Corresponding with this cathodic current, the resonant frequency in Figure 5b decreases (increase in electrode mass). The anodic/cathodic current and the mass loss/gain are reversible with cycling potential.

The correlation between mass gain and the cathodic current indicates that cations are mediating the charge storage. As the potential is swept in the negative direction, electrons enter the electrode and balance the charge of incoming cations. These results support previous assertions that cation intercalation is responsible for charge storage in MnO_2 .^{23,27,44} The observed slight hysteresis in the frequency trace in Figure 5b also indicates a slight lag in mass change as the total charge changes.

The mass change during electrochemical cycling can be estimated using the simplified Sauerbrey Equation, where $\Delta m = 56.6 \frac{\mu\text{g}}{\text{cm}^2 \text{ Hz}} \Delta f$.⁴⁵ The change in mass versus the change in accumulated charge at a sweep rate of 20 mV/s is consistent with a mass-to-charge ratio of -24.9 g/mol e^- for the cations. This mass-to-charge ratio of -24.9 g/mol e^- is close to the ratio of -23 g/mol e^- expected if Na^+ is the charge carrier. However, these EQCM results depend on the viscoelastic properties of the MnO_2 film.⁴⁵⁻⁴⁷ The results in Figure 5 suggest that cations with a mass close to that of Na^+ are involved in charge storage. Additional measurements are needed to confirm that Na^+ is the charge carrier.

Film composition and morphology after electrochemical oxidation.— XPS depth-profiling was employed to determine the composition of the MnO_2 film after electrochemical oxidation and at various states of charge. In the first XPS experiment that determined the film stoichiometry, the sample was oxidized to $7 \text{ e}^-/\text{Mn}$ at potentials up to 1.2 V in 0.1 M Na_2SO_4 . The sample was cycled for 48 CV cycles and 40 galvanostatic cycles and stopped at 0 V versus Ag/AgCl at the end of a cathodic sweep. The sample was then removed from the electrolyte and dried at ambient conditions for >24 hours. A small section was cut from the stainless steel sample and loaded into the XPS analysis chamber. An argon ion beam was used to ion mill the sample for 1 minute intervals and XPS spectra were acquired between these intervals.

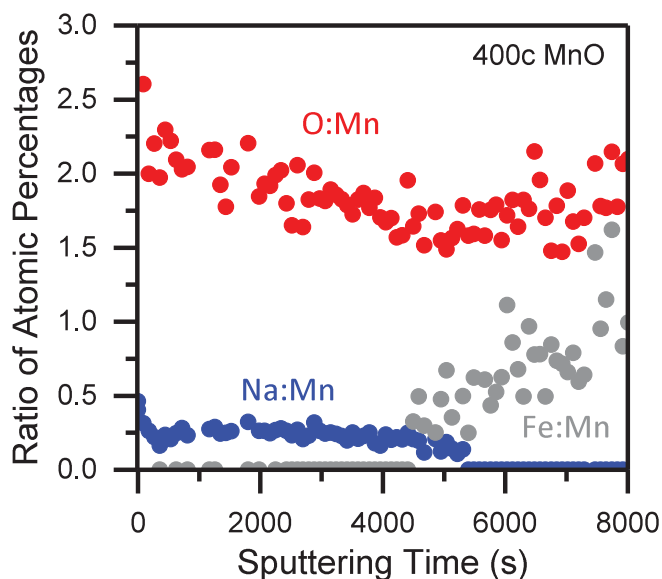


Figure 6. XPS intensity ratios for Na:Mn and O:Mn versus sputtering time during the XPS depth profile of a MnO_2 film formed by electrochemically oxidizing a MnO ALD film grown using 400 MnO ALD cycles.

The MnO_2 film contained a significant amount of Na throughout the depth of the film. The XPS signals were consistent with a bulk composition of $\text{Na}_{0.25}\text{MnO}_2$. The Na/Mn XPS signal ratio was ~ 0.25 and the O/Mn XPS signal ratio was ~ 2.0 , as shown in Figure 6. The rise of the Fe/Mn XPS ratio in Figure 6 indicates breakthrough into the underlying stainless steel. The sodium present in the MnO_2 film originates from the aqueous Na_2SO_4 electrolyte used during the electrochemical oxidation and CV and galvanostatic cycling.

Sodium ions in a 1:4 ratio with manganese are consistent with either $\alpha\text{-MnO}_2$ or $\delta\text{-MnO}_2$.⁴⁸ For these phases, the NaMn_4O_8 stoichiometry is consistent with sodium occupying every available interstitial site as shown in Figure 7. High concentrations of Na in MnO_2 contradict a prior report that observed very little sodium present in MnO_2 .⁴ However, this prior study only performed XPS on the electrode surface and did not interrogate the bulk. If the samples in the previous study were rinsed after electrochemical analysis, the rinsing could have led to a low concentration of sodium at the electrode surface. Additionally, differences in the amount of available surface area in this prior work and the work presented here may play a role in the amount of sodium observed by XPS.

A second set of XPS measurements were performed on electrochemically oxidized manganese oxide electrodes at various states of charge as presented in Figure 8. These MnO_2 samples were electro-

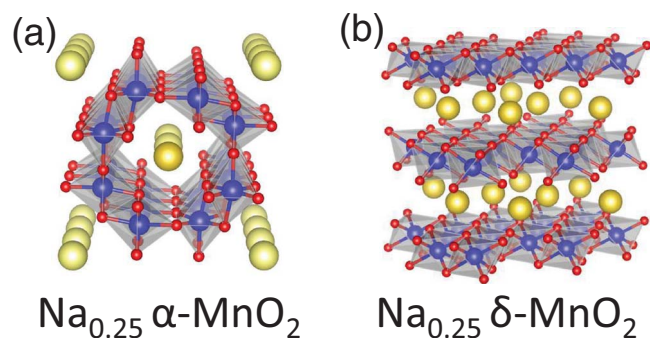


Figure 7. Crystal structures of (a) $\text{Na}_{0.25}\alpha\text{-MnO}_2$ and (b) $\text{Na}_{0.25}\delta\text{-MnO}_2$. Small red spheres indicate oxygen, medium blue spheres indicate manganese, and large yellow spheres indicate sodium.

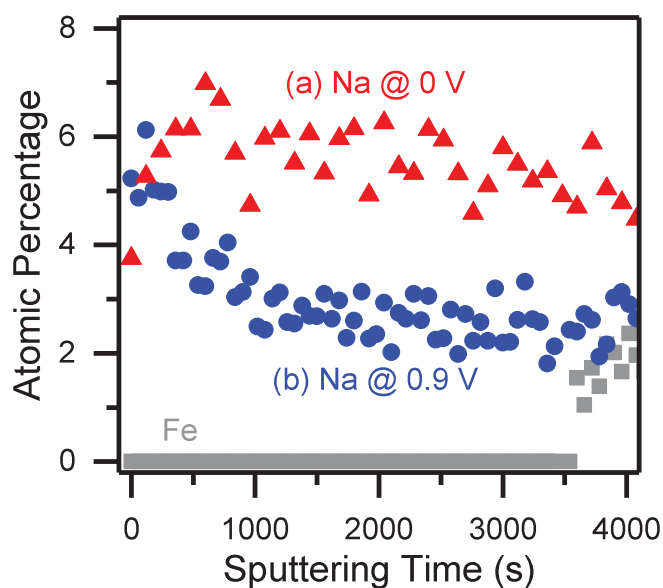


Figure 8. XPS measurements of atomic percentages of Na in MnO_2 films at different states of charge using the Na[1s] XPS signals. (a) Na at% after cathodic sweep and equilibration for 15 minutes at 0 V versus Ag/AgCl. (b) Na at% after anodic sweep and equilibration for 15 minutes at 0.9 V versus Ag/AgCl. Fe at% is zero until the sputter depth-profiling reaches the stainless steel support.

chemically oxidized at just over $2 e^-/\text{Mn}$ and at potentials up to 0.9 V. In these experiments, the amount of sodium in the MnO_2 films depends on the potential at which the electrode was held before the XPS measurements. In Figure 8a, the electrode was held at 0 V versus Ag/AgCl for 15 minutes. As shown in Figure 5, the sodium should be at its highest concentration in the MnO_2 film after the cathodic sweep when the potential is at 0 V versus Ag/AgCl. In Figure 8b, the electrode was held at 0.9 V versus Ag/AgCl for 15 minutes. As displayed in Figure 5, the sodium should be at its lowest concentration in the MnO_2 film after the anodic sweep when the potential is at 0.9 V versus Ag/AgCl.

Figure 8a shows that the Na^+ concentration is ~ 6 at% after the electrode is held at 0 V versus Ag/AgCl. In contrast, Figure 8b indicates that the Na^+ concentration is ~ 3 at% after the electrode is held at 0.9 V versus Ag/AgCl. This amount of sodium in the MnO_2 film at 0.9 V is only about half as much as the sodium in the MnO_2 film at 0 V. This behavior is consistent with the loss of mass observed by the EQCM measurement in Figure 5b after the anodic sweep to 0.9 V, as shown in Figure 5a.

However, the sodium removed from the MnO_2 film does not correspond to the total charge transferred during the CV experiment. A total charge of $\sim 0.2 \text{ mol } e^-/\text{mol Mn}$ was transferred during the anodic/oxidizing potential sweep in the CV experiment. This total charge storage agrees with a measured bulk sodium concentration of $\sim 0.2 \text{ mol Na/mol Mn}$ for a MnO_2 film held at a reducing potential of 0 V versus Ag/AgCl. However only about half of the sodium, or $\sim 0.1 \text{ mol Na/mol Mn}$, is measured to diffuse out of the electrode when held at an oxidizing potential of 0.9 V versus Ag/AgCl. This observation suggests that as much as 50% of the charge storage in the MnO_2 film does not require Na^+ diffusion. The remainder of the charge storage may arise from either proton-mediated processes^{1,4,26,27} or from electrons reversibly occupying bulk “charge-switching” states as predicted by recent theoretical work.²⁷

SEM micrographs for a stainless steel sample with 400 MnO ALD cycles before and after electrochemical oxidation are shown in Figure 9. The as-deposited MnO ALD film is pristine and flat, as shown in Figure 9a. There is some minor roughness on the order of tens of nanometers observed by atomic force microscopy (AFM). The AFM image is shown in the inset in Figure 9a. In contrast,

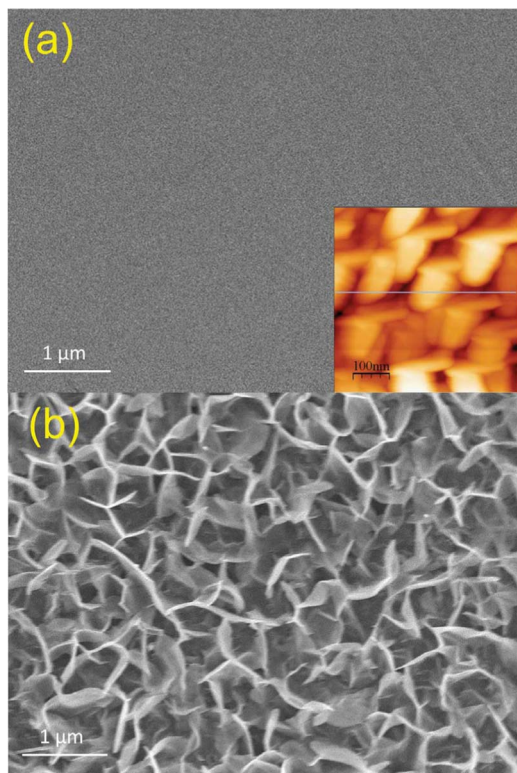


Figure 9. SEM micrograms of (a) MnO ALD film grown using 400 MnO ALD cycles on stainless steel and (b) MnO₂ film formed after electrochemical oxidation of MnO ALD film. Inset in (a) shows the atomic force microscopy image of the MnO ALD film.

Figure 9b shows that the Na_{0.25}MnO₂ film has a nanosheet morphology with ~1 μm features after electrochemical oxidation. This observed morphology change produces an increase in surface area. This higher surface area should increase the capacitance and charge storage by the MnO₂ films. The nanosheets may also lead to charge storage that is dependent on the thickness of the initial MnO ALD films.

Capacitance versus film thickness and sweep rate.— The areal capacitance, C_a , and the specific mass capacitance, C_m , after electrochemical oxidation are plotted versus number of MnO ALD cycles used to prepare the initial MnO ALD films in Figure 10. These capacitances correspond to a CV sweep rate of 20 mV/s and were calculated as average values using the total charge transferred over the scanned potential window. C_a was calculated using the area of the electrode exposed to the electrolyte during electrochemistry measurements. This area was $A = 1.21 \text{ cm}^2$. C_m was calculated using the mass of the MnO ALD films determined from the film thickness and density obtained by the XRR measurements and assuming that all of the MnO was converted to MnO₂. The areal capacitance in Figure 10a increases monotonically up to 2,000 MnO ALD cycles. The areal capacitance is not expected to display a peak. If additional film thickness contributes no capacitance, then the areal capacitance reaches a constant value.

The specific mass capacitance plotted in Figure 10b shows a maximum at 400 MnO ALD cycles. This behavior indicates that additional MnO₂ thickness contributes an increasing amount to the capacitance for initial MnO ALD thicknesses up to 40 nm obtained after 400 MnO ALD cycles. For initial MnO ALD films thicker than 40 nm, additional MnO₂ makes progressively smaller contributions to the capacity. The specific mass capacitance reaches a peak at 400 MnO ALD cycles and then decreases because additional film thickness contributes less capacitance. The decrease results from dividing by progressively larger masses.

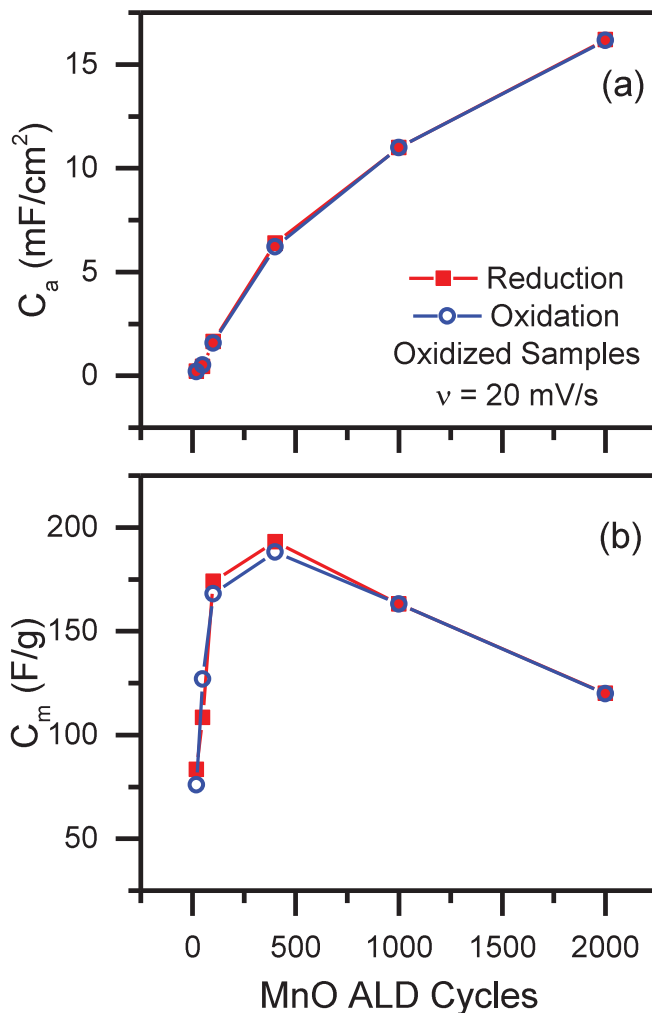


Figure 10. (a) Areal capacitance and (b) specific mass capacitance of MnO₂ films after electrochemical oxidation of MnO ALD films grown with various number of MnO ALD cycles. The capacitances were measured at a sweep rate of 20 mV/s.

Variation of the sweep rate for each MnO₂ thickness changes the measured areal capacitance and specific mass capacitance as shown in Figure 11. The capacity at a given sweep rate depends on the timescales of the various processes that contribute to the measured current. Figure 11a shows that for all sweep rates, the areal capacitance increases with increasing film thickness. This behavior indicates a contribution to charge storage from the entire MnO₂ film thickness. However, doubling the initial MnO ALD film thickness from 100 nm to 200 nm (1,000 MnO ALD cycles to 2,000 MnO ALD cycles) for a fast sweep rate of 400 mV/s only increases the areal capacitance by 10%. These results are consistent with a kinetic bottleneck for bulk charge storage in these thicker films.

The specific mass capacitances for each film versus sweep rate are displayed in Figure 11b. For initial MnO ALD films deposited using 100 MnO ALD cycles, the specific capacitance is 260 F/g at a sweep rate of 5 mV/s and decreases to 83 F/g at 400 mV/s. This drop in capacitance with increased sweep rate suggests that slow electrochemical processes are able to store large amounts of charge. Partial film dissolution in aqueous electrolyte prevents the thin MnO₂ films with thicknesses < 40 nm from approaching the highest reported capacitances of > 1,000 F/g at CV sweep rates of 5 mV/s.^{4,22} This film dissolution occurs during electrochemical oxidation and CV of the MnO₂ samples in aqueous electrolyte and is not accounted for in the calculation of specific mass capacitance. The local atomic structure,

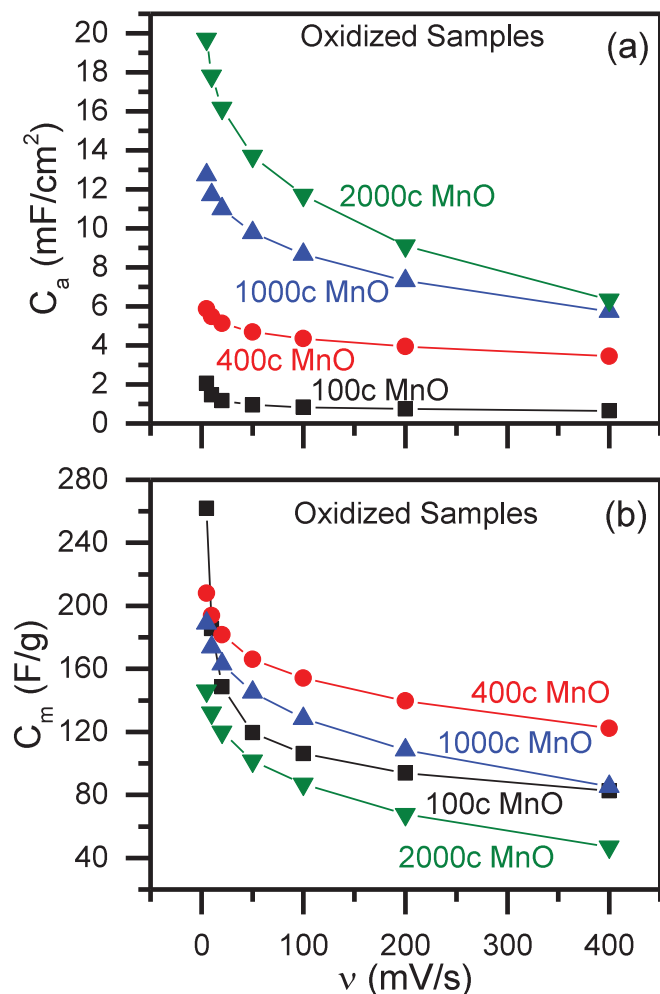


Figure 11. a) Areal capacitance and (b) specific mass capacitance of MnO₂ films versus sweep rate after electrochemical oxidation of MnO ALD films grown with various number of MnO ALD cycles.

morphology, or surface termination of our films may also impact their specific capacitance. These possible impacts are obscured by the known dissolution. We also note that a 5 mV/s CV sweep rate is uninteresting for supercapacitor applications, which require sweep rates ≥ 15 mV/s (≥ 60 C charge rates) for a 0.9 V potential window.⁴⁹

The MnO₂ film formed from the initial MnO ALD film grown with 400 MnO ALD cycles exhibits the highest specific mass capacitances for all sweep rates > 5 mV/s. This MnO₂ film has a specific capacitance of 208 F/g at 5 mV/s and maintains a specific capacitance of > 120 F/g even at a very high sweep rate of 400 mV/s. The data in Figure 11 suggests that this MnO₂ film may be an optimum thickness to maximize high-rate charge storage from MnO₂ films.

Energy and power densities from galvanostatic measurements.—Galvanostatic measurements were also performed on a MnO₂ film prepared from a MnO ALD film deposited with 400 MnO ALD cycles and then electrochemically oxidized to MnO₂. This MnO₂ film was chosen because this film exhibited the highest measured specific mass capacitance at high sweep rates in CV measurements. A plot of potential versus time for currents up to 100 μ A is shown in Figure 12. The symmetric and nearly triangular shape of the potential versus time measurements at various charge-discharge currents is ideal for a pseudocapacitive electrode. This ideal triangular shape is observed even for cycling times of < 60 seconds (> 60 C charge rate) at 100 μ A currents.

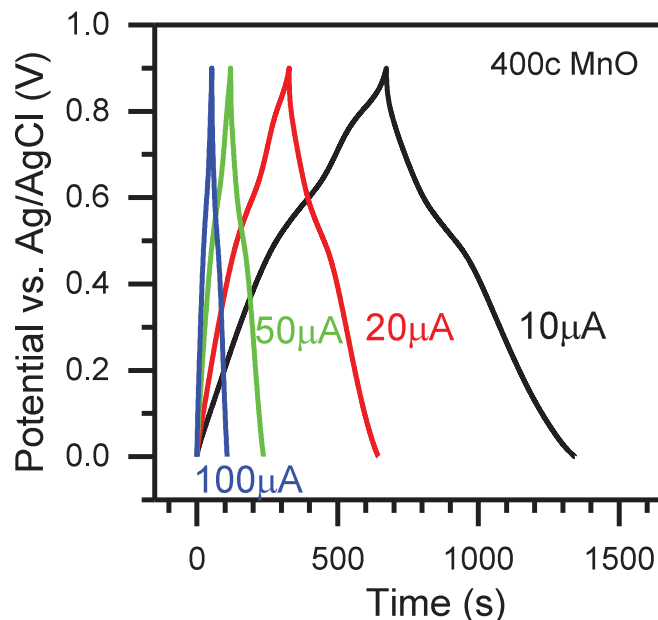


Figure 12. Galvanostatic plots of voltage versus time for charge and discharge currents of 10, 20, 50 and 100 μ A. The MnO₂ film was prepared by electrochemical oxidation of a MnO ALD film grown using 400 MnO ALD cycles.

The energy and power densities of the MnO₂ film at various charge-discharge currents are presented in the Ragone plot displayed in Figure 13. An energy density of > 35 Wh/kg is maintained for power densities of $> 1,000$ W/kg. This energy density is an order of magnitude above energy densities reported for state-of-the-art supercapacitor devices.^{1,2} With efficient scale-up, a MnO₂ film with a thickness of ~ 40 nm prepared by the electrochemical oxidation of a MnO ALD film deposited using 400 MnO ALD cycles could be employed to fabricate devices with an energy density significantly above state-of-the-art electrochemical capacitors.^{1,2}

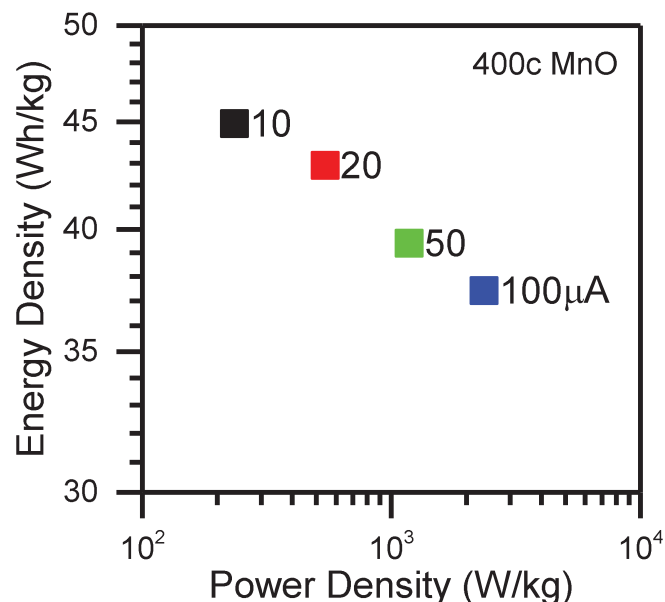


Figure 13. Ragone plot of energy density versus power density for the charge and discharge currents of 10, 20, 50 and 100 μ A shown in Figure 12.

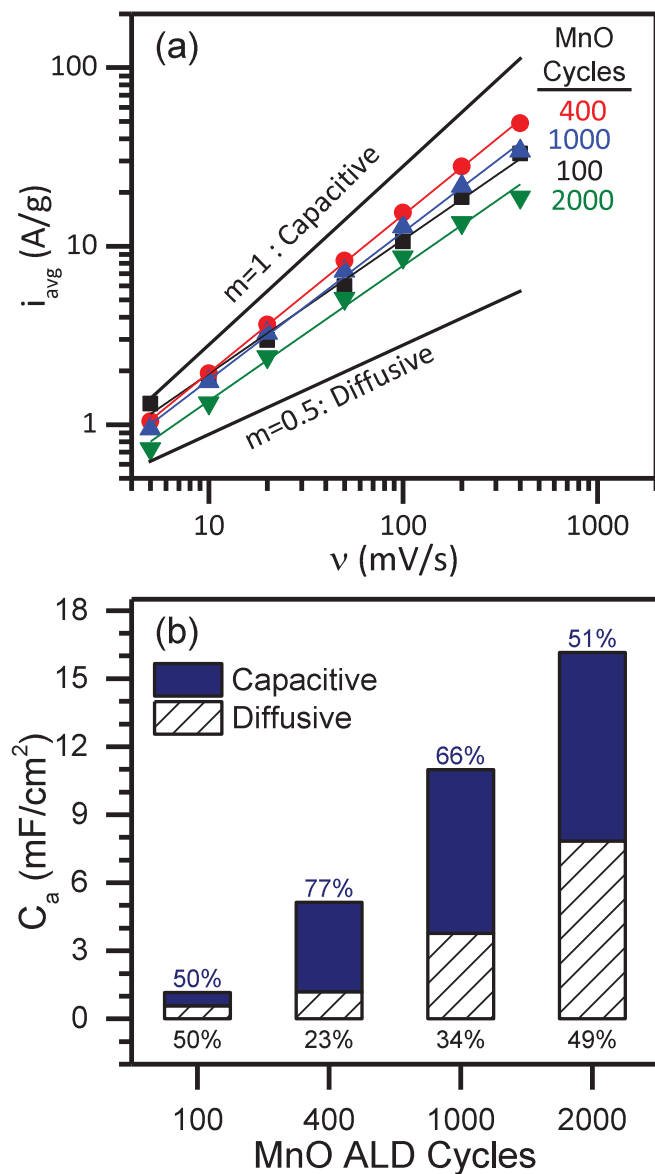


Figure 14. (a) Log-log plot of average oxidation current normalized by mass versus the sweep rate. Theoretical sweep rate dependencies for double-layer capacitance and diffusion-limited processes are shown for comparison. (b) Areal capacitance measured at 20 mV/s and separated into capacitive and diffusive components for MnO₂ films prepared by electrochemical oxidation of MnO ALD films.

Separating capacitive and diffusive processes.— The mass-averaged current is plotted versus sweep rate on the log-log plot shown in Figure 14 for various MnO₂ films formed from the electrochemical oxidation of MnO ALD films. The mass-averaged current was defined using the mass of MnO films determined from XRR thickness and density and assuming all of the MnO was converted to MnO₂. Figure 14 also shows the slopes expected for the limiting cases of capacitive ($i \propto v$) and diffusion limited ($i \propto v^{0.5}$) processes. Capacitive processes can include the surface electric double layer, dielectric polarization, and rapid “charge-switching” in the bulk.²⁷ Diffusive processes are limited by mass transport of ions from the electrolyte to the MnO₂ or in the MnO₂ bulk.

From Figure 14, the capacity arising from capacitive and diffusive processes can be separated using the expression

$$i = av^b \quad [1]$$

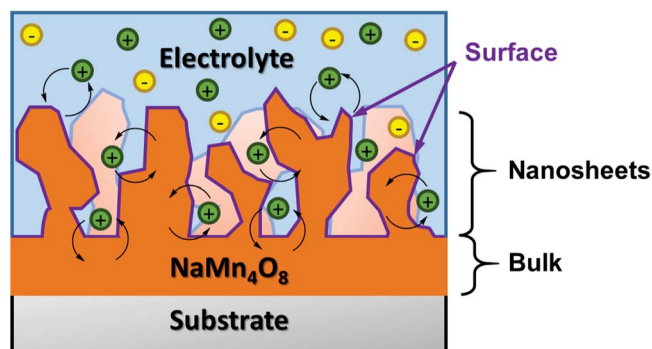


Figure 15. Schematic illustrating charge storage by MnO₂ films prepared by the electrochemical oxidation of MnO ALD films. Charge can be stored on the MnO₂ surface, in the MnO₂ nanosheets or in the MnO₂ bulk.

where a and b are constants, and the exponent, b , is bounded by 0.5 and 1, corresponding to diffusive and capacitive processes, respectively.⁵⁰ By assuming constant phase element (CPE) behavior for the underlying charge-storage processes,⁵¹ the value of b can vary freely between 0.5 and 1. By setting

$$b = 1 - 0.5 f_d \quad [2]$$

where f_d is the fraction of the capacity contributed by diffusive processes, the fractions of the capacity arising from capacitive and diffusive processes are determined and plotted in Figure 14b. This analysis is comparable to previous analyses that plotted $i/v^{0.5}$ versus $v^{0.5}$ by Wang⁵⁰ and q versus $v^{-0.5}$ by Ardizzone.⁵² See Supplementary Material for additional detail.⁵³

The MnO₂ film formed by oxidizing the MnO ALD film grown using 400 MnO ALD cycles shows the highest capacitive character. The analysis indicates that 77% of the capacity results from capacitive processes and that the capacity is not mass transport limited. Much of this capacitive charge storage likely arises from surface electric double layer processes. In support of substantial charge storage in the electric double layer, the SEM images reveal high surface area films after electrochemical oxidation.

The diffusive contribution to the capacity increases for the thicker MnO₂ films grown using 1,000 and 2,000 MnO ALD cycles. This growing diffusive contribution to charge storage is evidence for bulk charge storage. The increasing areal capacitance and growing diffusive contribution to the capacity argue strongly for bulk charge storage in MnO₂. The conclusion that there is significant bulk charge storage in MnO₂ is at odds with the view that charge storage in MnO₂ is primarily a surface effect. However, many prior studies have reported that charge storage in MnO₂ may be occurring in the bulk.^{20–26,54}

A schematic illustrating charge storage in MnO₂ is shown in Figure 15. This schematic is based on the CV, EQCM, XPS and SEM results and the analysis of the capacitive and diffusive processes. Charge can be stored on the MnO₂ surface, in the MnO₂ nanosheets or in the MnO₂ bulk. The MnO₂ nanosheets may allow the surface area to increase progressively with the thickness of the initial MnO ALD film. The MnO₂ nanosheets may not account for as large a fraction of the MnO₂ films prepared from initial MnO ALD films grown using >400 MnO ALD cycles. This more bulk-like MnO₂ leads to an increase in the fraction of diffusive charge transfer.

Conclusions

MnO₂ electrochemical supercapacitor electrodes were fabricated by the electrochemical oxidation of MnO ALD films. CV analysis confirmed that oxidation of MnO to MnO₂ involved 2 moles of electrons per mole Mn in the initial MnO ALD film. The capacity of the initial MnO ALD films increased progressively with electrochemical oxidation to MnO₂ films. SEM images revealed that the MnO₂ films produced by electrochemical oxidation exhibited a nanosheet

morphology that increases their surface area. XPS depth-profile analysis showed that after the reducing/cathodic potential sweeps the MnO₂ films contain sodium with a stoichiometry of Na_{0.25}MnO₂.

EQCM measurements were consistent with cations as the primary charge storage species in MnO₂. The observed mass-to-charge ratio of -24.9 g/mol e^- was very close to the ratio of -23 g/mol e^- expected if Na⁺ is the charge carrier. However, the viscoelastic properties of the MnO₂ nanosheets preclude a quantitative determination of the exact mass of the cation species. XPS experiments also measured sodium in MnO₂ after both positive/anodic and negative/cathodic voltage sweeps. Approximately one-half of the sodium was removed after the positive/anodic voltage sweeps. A comparison of sodium removed and charge transferred indicated that approximately one-half of the charge is accounted for by sodium transport in and out of the MnO₂. The other one-half of the charge may be attributed to hydrogen ions or “charge switching” interstitial and substitutional cations in MnO₂.

The capacity was dependent on the initial number of MnO ALD cycles used to prepare the MnO₂ films. The specific mass capacitance reached a peak at $\sim 180 \text{ F/g}$ at 20 mV/s for MnO₂ films formed from initial MnO ALD films grown using 400 MnO ALD cycles. The thinner MnO₂ films displayed a higher specific capacitance of $>200 \text{ F/g}$ at 5 mV/s. Experiments at various scan rates indicated that charge storage in MnO₂ originates from a combination of capacitive and diffusive processes. While a portion of this capacity likely originates from the surface double layer, the increasing diffusive contribution from MnO₂ films formed from thicker initial MnO ALD films argues that bulk charge storage makes a sizeable contribution to the total charge storage of MnO₂. This picture is in contrast to the generally held view that charge storage in pseudocapacitors is dominated by surface charge storage. The high levels of charge storage, the high charge/discharge rates and the reversibility of the charge incorporation are very promising for applications for MnO₂ as a cathode material for sodium-ion batteries or for battery-inspired water desalination.

Acknowledgments

This work was supported by the Defense Advanced Research Project Agency (DARPA) and the National Science Foundation through a Graduate Research Fellowship under grant No. DGE 1144083. C.B.M. acknowledges support from the NSF through grant CHE-1214131. Any opinion, findings, and conclusions or recommendations expressed in this material are those of the authors and do not necessarily reflect the views of the NSF. We thank Dr. Luda Wang from the Department of Mechanical Engineering at the University of Colorado for Atomic Force Microscopy measurements and Tomoko Borsa from the Nano Characterization Facility at the University of Colorado Boulder for assistance with SEM measurements.

References

- P. Simon and Y. Gogotsi, *Nat. Mater.*, **7**, 845 (2008).
- P. J. Hall, M. Mirzaei, S. I. Fletcher, F. B. Sillars, A. J. R. Rennie, G. O. Shitta-Bey, G. Wilson, A. Cruden, and R. Carter, *Energy Environ. Sci.*, **3**, 1238 (2010).
- M.-K. Song, S. Cheng, H. Chen, W. Qin, K.-W. Nam, S. Xu, X.-Q. Yang, A. Bongiorno, J. Lee, J. Bai, T. A. Tyson, J. Cho, and M. Liu, *Nano Lett.*, **12**, 3483 (2012).
- M. Toupin, T. Brousse, and D. Bélanger, *Chem. Mater.*, **16**, 3184 (2004).
- D. Bélanger, L. Brousse, and J. Long, *Electrochem. Soc. Interface*, **Spring**, 49 (2008).
- T. Brezesinski, J. Wang, S. H. Tolbert, and B. Dunn, *Nat. Mater.*, **9**, 146 (2010).
- Q. Huang, X. Wang, J. Li, C. Dai, S. Gamboa, and P. J. Sebastian, *J. Power Sources*, **164**, 425 (2007).
- S. Hadzi-Jordanov, H. Angerstein-Kozłowska, M. Vukovic, and B. E. Conway, *J. Electrochem. Soc.*, 1471 (1978).
- S. Hwang and S. Hyun, *J. Power Sources*, **172**, 451 (2007).
- T. Brezesinski, J. Wang, S. H. Tolbert, and B. Dunn, *J. Sol-Gel Sci. Technol.* (2010).
- C.-T. Hsieh, C.-C. Chang, W.-Y. Chen, and W.-M. Hung, *J. Phys. Chem. Solids*, **70**, 916 (2009).
- X. Sun, M. Xie, G. Wang, H. Sun, A. S. Cavanagh, J. J. Travis, S. M. George, and J. Lian, *J. Electrochem. Soc.*, **159**, A364 (2012).
- S. Boukhalfa, K. Evanoff, and G. Yushin, *Energy Environ. Sci.*, **5**, 6872 (2012).
- I.-H. Kim, J.-H. Kim, B.-W. Cho, and K.-B. Kim, *J. Electrochem. Soc.*, **153**, A1451 (2006).
- I.-H. Kim, J.-H. Kim, B.-W. Cho, Y.-H. Lee, and K.-B. Kim, *J. Electrochem. Soc.*, **153**, A989 (2006).
- Y. Zhang, H. Li, L. Pan, T. Lu, and Z. Sun, *J. Electroanal. Chem.*, **634**, 68 (2009).
- T. Lu, Y. Zhang, H. Li, L. Pan, Y. Li, and Z. Sun, *Electrochim. Acta*, **55**, 4170 (2010).
- S. Sarangapani, *J. Electrochem. Soc.*, **143**, 3791 (1996).
- T. Brousse, D. Bélanger, and J. W. Long, *J. Electrochem. Soc.*, **162**, A5185 (2015).
- S. Devaraj and N. Munichandraiah, *J. Phys. Chem. C*, **112**, 4406 (2008).
- T. Brousse, M. Toupin, R. Dugas, L. Athouël, O. Crosnier, and D. Bélanger, *J. Electrochem. Soc.*, **153**, A2171 (2006).
- W. Yan, J. Y. Kim, W. Xing, K. C. Donovan, T. Ayvazian, and R. M. Penner, *Chem. Mater.*, **24**, 2382 (2012).
- S.-L. Kuo and N.-L. Wu, *J. Electrochem. Soc.*, **153**, A1317 (2006).
- S.-F. Chin, S.-C. Pang, and M. A. Anderson, *J. Electrochem. Soc.*, **149**, A379 (2002).
- S.-C. Pang, M. A. Anderson, and T. W. Chapman, *J. Electrochem. Soc.*, **147**, 444 (2000).
- S. Wen, J. Lee, I. Yeo, J. Park, and S. Mho, *Electrochim. Acta*, **50**, 849 (2004).
- M. J. Young, A. M. Holder, S. M. George, and C. B. Musgrave, *Chem. Mater.*, **27**, 1172 (2015).
- B. E. Conway, *Electrochemical supercapacitors: scientific fundamentals and technological applications*, Springer (1999).
- O. Nilsen, H. Fjellvåg, and A. Kjekshus, *Thin Solid Films*, **444**, 44 (2003).
- O. Nilsen, S. Foss, H. Fjellvåg, and A. Kjekshus, *Thin Solid Films*, **468**, 65 (2004).
- B. B. Burton, F. H. Fabreguette, and S. M. George, *Thin Solid Films*, **517**, 5658 (2009).
- J. W. Elam, M. D. Groner, and S. M. George, *Rev. Sci. Instrum.*, **73**, 2981 (2002).
- P. Taylor, *Crystallographic Databases*, International Union of Crystallography, (1988), p. 1153.
- A. Jain, S. P. Ong, G. Hautier, W. Chen, W. D. Richards, S. Dacek, S. Cholia, D. Gunter, D. Skinner, G. Ceder, and K. a. Persson, *APL Mater.*, **1**, 011002 (2013).
- F. Izumi, *Solid State Ionics*, **172**, 1 (2004).
- K. Momma and F. Izumi, *J. Appl. Crystallogr.*, **44**, 1272 (2011).
- S. Lany, *Phys. Rev. B*, **87**, 085112 (2013).
- C. Franchini, R. Podloucky, J. Paier, M. Marsman, and G. Kresse, *Phys. Rev. B*, **75**, 1 (2007).
- Malvern Instruments Ltd, *Sample dispersion & refractive index guide*, Malvern, Worcestershire, U.K., (1997).
- R. D. Shannon, *J. Phys. Chem. Ref. Data*, **31**, 931 (2002).
- L. Mai, H. Li, Y. Zhao, L. Xu, X. Xu, Y. Luo, Z. Zhang, W. Ke, C. Niu, and Q. Zhang, *Sci. Rep.*, **3**, 1718 (2013).
- B. P. Hahn, J. W. Long, and D. R. Rolison, *Acc. Chem. Res.*, **46**, 1181 (2013).
- D. P. Dubal, D. S. Dhawale, R. R. Salunkhe, and C. D. Lokhande, *J. Electrochem. Soc.*, **157**, A812 (2010).
- C. Sun, Y. Zhang, S. Song, and D. Xue, *J. Appl. Crystallogr.*, **46**, 1128 (2013).
- D. A. Buttry, *Electroanal. Chem. - A Ser. Adv.*, **17**, 1 (1991).
- M. R. Deakin, D. A. Buttry, M. R. Deakln, and D. A. Bulq, *Anal. Chem.*, **61**, 1147A (1989).
- R. Borjas and D. A. Buttry, *J. Electroanal. Chem. Interfacial Electrochem.*, **280**, 73 (1990).
- L. Gmelin, in *Verlag Chemie, GmbH Weinheim/Bergstrasse*, E. Schleitzer-Steinkopf, Editor, p. 170, Verlag Chemie - GMBH, Weinheim (1973).
- P. Simon, Y. Gogotsi, and B. Dunn, *Science*, **343**, 1210 (2014).
- J. Wang, J. Polleux, J. Lim, and B. Dunn, *J. Phys. Chem. C*, **111**, 14925 (2007).
- M. E. Orazem and B. Tribollet, *Electrochemical Impedance Spectroscopy*, John Wiley & Sons, Hoboken, New Jersey, (2008), p. 1.
- S. Ardizzone, G. Fregonara, and S. Trasatti, *Electrochim. Acta*, **35**, 263 (1990).
- See supplementary information at <http://dx.doi.org/10.1149/2.0671514jes> for additional information.
- O. Ghodbane, F. Ataherian, N.-L. Wu, and F. Favier, *J. Power Sources*, **206**, 454 (2012).